Infrared phonon spectroscopy on the Cairo pentagonal antiferromagnet $Bi_2Fe_4O_9$: A study through the pressure-induced structural transition

M. Verseils [1], A. P. Litvinchuk [2], J-B. Brubach,[1] P. Roy [1], K. Beauvois,[3] E. Ressouche [4], V. Skumryev,[5] M. Gospodinov,[6]
V. Simonet,[7] and S. de Brion[7]

[1]*Ligne AILES - Synchrotron SOLEIL, 91190 Gif-sur-Yvette CEDEX, France*
[2]*Texas Center for Superconductivity, University of Houston, Houston, Texas 77204, USA*
[3]*Université Grenoble Alpes, CEA, IRIG, MEM, MDN, 38000 Grenoble, France and Institut Laue-Langevin, 38000 Grenoble, France*
[4]*INAC/MEM, CEA-Grenoble, 38042 Grenoble, France*
[5]*Institució Catalana de Recerca i Estudis Avançats (ICREA), 08010 Barcelona, Spain and Departament de Física, Universitat Autònoma de Barcelona, 08193 Bellaterra, Spain*
[6]*Institute of Solid State Physics, Bulgarian Academy of Sciences, 1784 Sofia, Bulgaria*
[7]*Université Grenoble Alpes, CNRS, Institut Néel, 38000 Grenoble, France*

Magnetic and crystallographic transitions in the Cairo pentagonal magnet $Bi_2Fe_4O_9$ are investigated by means of infrared synchrotron-based spectroscopy as a function of temperature (20–300 K) and pressure (0–15.5 GPa). One of the phonon modes is shown to exhibit an anomalous softening as a function of temperature in the antiferromagnetic phase below 240 K, highlighting spin-lattice coupling. Moreover, under applied pressure at 40 K, an even larger softening is observed through the pressure-induced structural transition. Lattice dynamical calculations reveal that this mode is indeed very peculiar as it involves a minimal bending of the strongest superexchange path in the pentagonal planes, as well as a decrease in the distances between second-neighbor irons. The latter confirms the hypothesis made by Friedrich *et al.*, [J. Phys.: Condens. Matter **24**, 145401 (2012)] about an increase in the oxygen coordination of irons being at the origin of the pressure-induced structural transition. As a consequence, one expects a new magnetic superexchange path that may alter the magnetic structure under pressure.

I. INTRODUCTION

The Cairo pentagonal lattice is an original network containing irregular pentagons that are connected by their edges via threefold and fourfold connected sites (see Fig. 1). It has attracted interest lately because the pentagon building block has an odd number of bonds which can promote magnetic frustration as in the intensively studied triangle-based networks [1]. In such frustrated magnets, it has been predicted and observed experimentally that the stabilization of a long-range magnetic order may be impeached in favor of fluctuating states down to the lowest temperature, an archetypical example being the spin ice state on the pyrochlore lattice [2]. When the frustration can be partly released, thanks to other degrees of freedom such as lattice distortion, for instance, complex magnetic order (noncollinear) may prevail [3,4]. These complex magnetic phases can furthermore induce a ferroelectric order when they break the centrosymmetry: These are type II multiferroics that have attracted considerable interest over the past 15 years [5–11].

In this paper, we focus on one of the few experimental realizations of a Cairo pentagonal lattice, the bismuth iron oxide $Bi_2Fe_4O_9$ [12]. At ambient conditions, this compound crystallizes in the orthorhombic space group *Pbam*, No. 55, with 2 f.u. per unit cell. This unit cell (see Fig. 1) contains two distinct sites, Fe1 and Fe2, occupied by four Fe^{3+} ions

each, which have different oxygen coordinations (tetrahedral for Fe1 and octahedral for Fe2). The whole Fe network forms an analog of the Cairo pentagonal lattice in the *ab* plane with the noticeable difference that the fourfold connected site in the perfect lattice is replaced by a pair of Fe2 ions stacked along the *c* axis and sandwiching the planes containing the Fe1 ions (see left panel of Fig. 1). The compound orders antiferromagnetically below $T_N = 238$ K in a complex noncollinear magnetic structure formed by two interlocked sublattices associated with the two different Fe1 and Fe2 sites where the spins are at 90° with respect to each other (see Fig. 1) [12]. This remarkable magnetic arrangement is a direct signature of competing interactions and complex connectivity, which has been confirmed by theoretical studies [13,14]. In $Bi_2Fe_4O_9$, the magnetic structure remains centrosymmetric, and no associated ferroelectric order is expected although it has been reported for polycrystalline samples or nanoparticles [15,16].

Another interesting result concerning this material is that an isostatic pressure alters the crystallographic arrangement: Above 7 GPa, Friedrich *et al.* [17] have reported a pressure-induced structural transition at room temperature from *Pbam* to *Pbnm* (No. 62) centrosymmetric space groups with the doubling of the unit cell along the *c* axis ($c' = 2c$). The driving force of the transition was proposed to arise from the tendency of tetrahedral Fe1 to increase their oxygen coordination to
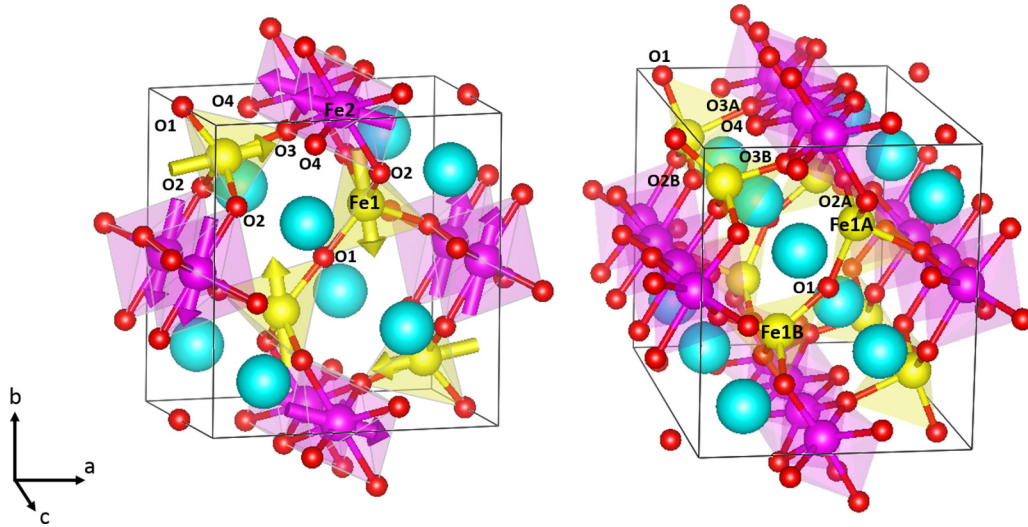
FIG. 1. Left: The orthorhombic *Pbam* unit cell of $Bi_2Fe_4O_9$ at low temperature and ambient pressure conditions. The arrows represent the spin orientation in the magnetic ordered phase (T < T_N) [12]. Right: The orthorhombic *Pbnm* unit cell of $Bi_2Fe_4O_9$ at high pressure (P > 7 GPa) and room temperature [17]. Blue, bismuth atoms; yellow, tetrahedral irons (Fe1); pink, octahedral irons (Fe2); red, oxygens.

5 under pressure. Another clear signature of the transition is the large displacement of the O1 oxygen atoms that connect two Fe1 tetrahedra [17] (see Fig. 1). This pressure-induced structural transition raises the issue of its influence on the magnetic order observed at ambient pressure below 238 K, since it might strongly affect the magnetic superexchange paths enabling this order.

To gain better insight into this material, we have investigated the temperature and pressure evolution of the phonon modes that involve atomic displacements within the pentagonal plane by means of infrared (IR) measurements. For this purpose, we have used the intense infrared source available on the AILES-B beamline at synchrotron SOLEIL combined with two different setups, one adapted to bulk sample allowing low-temperature measurements at ambient pressure and the second for high-pressure and low-temperature measurements adapted to submillimeter crystals [18]. We have been able to identify all the B_{2u} infrared phonon modes and to follow their evolution through the structural and magnetic phase transitions. We evidenced magnetoelastic effects comparable to what is usually observed in antiferromagnets [19–23]. Finally, we show that at least one mode, around 225 cm^{-1}, has an abnormal behavior both as a function of temperature and as a function of pressure, whose implication for the magnetic properties is discussed.

II. EXPERIMENT

Single crystals of $Bi_2Fe_4O_9$ were synthesized using the high-temperature solution growth method as described elsewhere [24]. Crystals were then preoriented using a Rigaku Xcalibur S four-circle x-ray diffractometer.

The infrared spectroscopy measurements were performed in the reflectivity configuration on the IFS125MR Michelson interferometer installed on the AILES beamline at SOLEIL. A 6-μm Mylar beamsplitter and a 4.2-K bolometer were used to perform measurements in the far-infrared (FIR) (60–850 cm^{-1}) range with a resolution of 2 cm^{-1}. Measure-

ments at ambient pressure on bulk sample were performed between room temperature and 20 K using a helium closed-cycle cryostat. The optical setup allows a strong focusing and a quasinormal incidence of the synchrotron beam onto the sample surface. The FIR waves were linearly polarized thanks to a polyethylene polarizer. The absolute reflectivity of the sample was obtained by using as reference the same gold-coated sample obtained by *in situ* gold coating evaporation technique [25].

High-pressure measurements were realized at 40 K in the quasinormal reflectivity geometry inside a diamond anvil cell (DAC) plugged into a cryostat in a high-pressure/low-temperature box [18]. The diameter of the culets of the diamond anvil was 500 μm. A stainless steel gasket was preindented and then drilled to allow us to get a 250-μm-wide and 50-μm-deep hole adapted to the sample size. This latter was preoriented and polished to be 30 μm thick with a Leica mechanical polisher. Polyethylene powder was used as the transmitting medium to fill the hole, and a ruby ball was placed next to the sample to allow *in situ* determination of the pressure using fluorescence. The reflectivity of a gold foil in place of the sample at room temperature was used as the reference.

III. RESULTS

A. Γ-point IR phonons

Group theory predicts $\Gamma_{Raman} = 12$ $A_g + 12$ $B_{1g} + 9$ $B_{2g} + 9$ $B_{3g} = 42$ Raman active modes, $\Gamma_{IR} = 8$ $B_{1u} + 14$ $B_{2u} + 14$ $B_{3u} = 36$ infrared active modes, and 9 A_u silent modes in the low-pressure *Pbam* space group and 25 $A_g + 20$ $B_{1g} + 25$ $B_{2g} + 20$ $B_{3g} = 90$ Raman active modes, 24 $B_{1u} + 19$ $B_{2u} + 24$ $B_{3u} = 67$ infrared active modes, and 20 A_u silent modes in the high-pressure *Pbnm* space group. At ambient pressure, for a FIR polarization along the *b* axis, a total of 14 infrared active B_{2u} modes are expected. The reflectivity spectrum obtained at ambient conditions with a FIR electric field along the *b* axis is
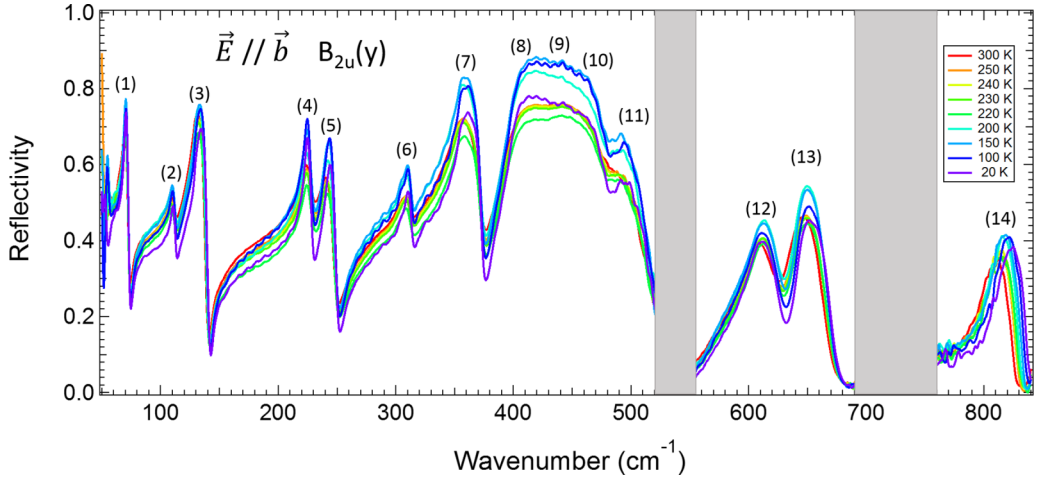
FIG. 2. Far-infrared reflectivity at quasinormal incidence of $Bi_2Fe_4O_9$ obtained at different temperatures, ambient pressure, and with the electric field **E** of the electromagnetic wave along the b axis of the sample. The two grayed out regions are not detectable because of destructive interferences of multiple reflections inside the beamsplitter. The numbers indicate the 14 B_{2u} infrared active modes detected as expected from group theory in this configuration.

presented in Fig. 2. Considering that the broad band between 400 and 500 cm^{-1} is composed of four unresolved modes, we are able to identify all 14 B_{2u} modes numbered in Fig. 2.

Lattice dynamical calculations (LDCs) for $Bi_2Fe_4O_9$ were performed within the shell model using the general utility lattice program (GULP) [26], which is known to adequately describe phonon modes of oxides with various crystallographic structures [27–30]. In the shell model, each ion is considered to be a point core surrounded by a massless shell. The free ion polarizability is accounted for by a force constant. The short-range potentials $V(r)$ are chosen in the Born-Mayer-Buckingham form as follows:

$$V(r) = a \exp(-r/r_0) - cr^6,$$

where r is the interatomic distance. The Coulomb energy calculations are based on a real-space summation involving a spherical cutoff boundary, which is defined by the cutoff radius (set to 12 Å), which makes the sum of all charges within the spherical cutoff region equal to zero. In our calculations, we used the same set of shell model parameters and short-range potentials, which provides frequencies closest to the experimental $Bi_2Fe_4O_9$ Raman scattering study [24]. The calculated frequencies and the main atomic motions involved in the infrared modes are given in Table I. All experimental frequencies, except those of modes (9)–(11), were obtained by fitting the data with REFFIT software [31] using the Drude-Lorentz (DL) model for the dielectric function of insulating materials, as described in the Appendix. We fitted the data under the constraint that the reflectivity calculated at normal incidence at the air-sample interface, $R = |1 - \sqrt{\epsilon}|^2/|1 + \sqrt{\epsilon}|^2$, matches the experimental value.

The assignment proposed in Table I allows us to identify all the 14 experimental modes. The modes associated with heavier atoms are located at the lower frequencies: The first mode, in particular, is attributed mainly to the Bi atom displacements, modes (2)–(6) are attributed to Fe and oxygen displacements, and displacements of the oxygens alone are involved in modes (7)–(14). The mean deviation between experimental and calculated phonon frequencies is found to

be 10%, which might be considered as reasonable, remembering that the parametric shell model does not take into account electronic correlations. Note that our measurements are in qualitative agreement with previous infrared studies on $Bi_2Fe_4O_9$ [32,33] that do not report any experimental modes above 850 cm^{-1} either.

B. Temperature dependence of IR phonons

Reflectivity measurements of $Bi_2Fe_4O_9$ between 20 and 300 K were performed at quasinormal incidence with the electric field along the b axis of the bulk sample. The reference for each spectrum is the reflectivity of the sample covered with gold measured at the same temperatures. As already known from previous studies [12,34], when lowering temperature, $Bi_2Fe_4O_9$ undergoes an antiferromagnetic transition at $T_N = 238$ K while no structural transition has

TABLE I. Frequencies of the B_{2u} infrared active modes of $Bi_2Fe_4O_9$ determined experimentally at 300 K and calculated. The corresponding main atomic motions are also reported.

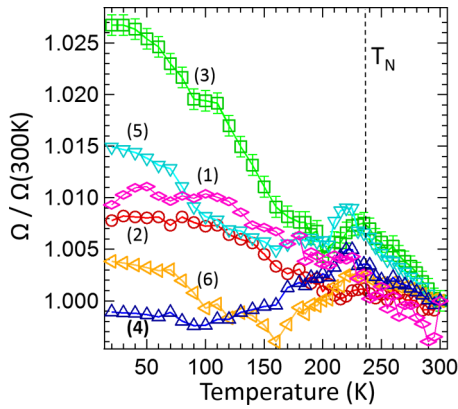| B_{2u} Mode	Expt. (cm^{-1})	LDC (cm^{-1})	Main atomic motions
(1)	69	93	Bi(y)
(2)	110	139	Fe1(xy)+O1(xy)
(3)	128	180	Fe1(y)+Fe2(y)+O1(y)+O2(xy) + O3(y)
(4)	225	202	Fe1(y)+Fe2(y)+O1(y)+O2(y)+O3(y)
(5)	238	290	Fe1(x)+Fe2(x)+O1(xy)+O3(y)+O4(x)
(6)	310	325	Fe1(x)+O1(xy)+O3(xy)
(7)	351	383	O2(x)+O3(x)+O4(xy)
(8)	399	409	O1(xy)+O2(y)+O3(x)
(9)	~430	450	O1(x)+O2(x)+O3(y)+O4(xy)
(10)	~455	499	Fe2(x)+O2(x)+O3(y)+O4(x)
(11)	~490	613	O1(x)+O2(xyz)+O3(xy)+O4(x)
(12)	605	639	O1(x)+O3(y)+O4(y)
(13)	645	789	O2(yz)
(14)	805	976	O1(xy)

FIG. 3. Temperature dependence of normalized frequencies Ω_k of modes $B_{2u}(1)$, $B_{2u}(2)$, $B_{2u}(3)$, $B_{2u}(4)$, $B_{2u}(5)$, and $B_{2u}(6)$ of $Bi_2Fe_4O_9$ from room temperature to 20 K. The reference is the frequency value at 300 K. The dashed line represents the Néel temperature of the sample, $T_N = 238$ K. For the sake of clarity, the error bars are given only for mode (3) and were estimated from the reproducibility of the fits by changing the number of modes in the model.

been reported. As expected, our measurements reported in Fig. 2 show that the number of modes (14 B_{2u}) is maintained through the whole temperature range. Here again, we used the DL model described previously and fitted the spectra at each temperature using REFFIT software [31]. The modes between 50 and 250 cm^{-1} can be fitted with high accuracy and small error bars at each temperature as they are narrow and well separated.

In Fig. 3, the normalized frequencies of modes (1)–(6) obtained from the DL model fits are displayed as a function of temperature. We also report all the fit parameters in the Appendix. The conventional temperature dependence of phonon modes is described by the well-known relations reported by Balkanski *et al.* [35]: Due to anharmonicity of the

potential, a progressive frequency hardening is expected with decreasing temperature, which levels off at low temperature. With the exception of modes (1) and (2), all modes show a pronounced deviation from the Balkanski's behavior, characterized by an abnormal softening starting just below T_N. The softening stops at 200 K for mode (3) and at 160 K for modes (5) and (6). At lower temperature, all these modes recover the conventional hardening. Noticeably, mode (4) starts to soften at T_N and never recovers the Balkanski's behavior at low temperature. These different softenings suggest that the antiferromagnetic interactions responsible for the long-range antiferromagnetic order below T_N affect the atomic displacements involved in modes (3)–(6) through spin-lattice coupling. This effect is maximal for mode (4), which displays a singular behavior with the strongest deviation from conventional phonon thermal evolution.

C. IR phonons under high pressure

In order to complete our study and to investigate the pressure-induced structural transition reported by Friedrich *et al.* [17], we measured the reflectivity of $Bi_2Fe_4O_9$ from 1 to 15.5 GPa with the electric field of the electromagnetic wave along the *b* axis at a temperature of 40 K (well below the reported antiferromagnetic transition at ambient pressure). These spectra are displayed in Fig. 4. They are in good agreement with the spectrum of the bulk measured as a function of temperature. Due to diffraction, multiple reflections inside the diamond anvil cell, and beamsplitter limitations, the low-frequency (under 100 cm^{-1}) and high-frequency (above 700 cm^{-1}) parts of the spectra are not usable. Therefore modes (1), (2), and (14) detected in the bulk sample are not visible in the high-pressure spectra of Fig. 4. Nevertheless, all the other modes detected in the bulk sample are recovered and are numbered as in Fig. 2. Interestingly, in the 1-GPa spectrum, we can identify unambiguously all four modes of the broad band between 450 and 550 cm^{-1}, which confirms our previous hypothesis.
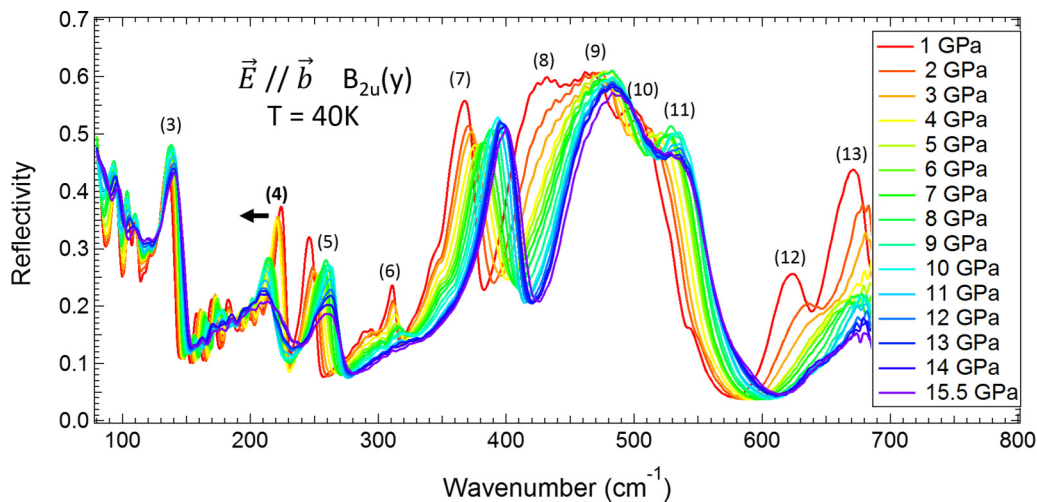

FIG. 4. Far-infrared reflectivity at quasinormal incidence of a small sample ($\sim$200 μm) of $Bi_2Fe_4O_9$ obtained in the diamond anvil cell and with electric field E of the electromagnetic wave along the *b* axis. The reference used is the reflectivity of a piece of gold leaf of approximately the same size as the sample and placed in the hole of the gasket of the DAC. The numbers indicate the B_{2u} infrared active modes already identified in the bulk sample.

According to Friedrich *et al.* [17], $Bi_2Fe_4O_9$ undergoes a structural transition from *Pbam* toward *Pbnm* with the doubling of the unit cell at about 7 GPa at ambient temperature. In the high-pressure space group *Pbnm* ($Z = 4$), group theory predicts 19 B_{2u} infrared active modes. We expect to observe, apart from the initial 14 B_{2u} singlet modes, 5 additional ones of the same symmetry. In contrast, our data show no additional modes when pressure is increased up to 15.5 GPa. From structural refinements of x-ray data under pressure [17], it is established that the lattice distortion in the *ab* plane is quite small and probably too weak to induce new infrared detectable phonons. Moreover, the shape of a phonon band measured by reflectivity can be quite large because of the spreading from transverse (resonance) to longitudinal frequencies thus causing overlapping of close modes. Note that some new modes have been observed by Raman spectroscopy at the pressure-induced transition [17], but not all the predicted ones. Our IR data evidence a substantial broadening of modes (4)–(6) with pressure. All the IR modes, with the noticeable exception of mode (4), shift toward higher frequencies with increasing pressure, as expected for a normal lattice contraction and hardening of forces between atoms.

As described by Langerome *et al.* [36], the interface with a diamond affects the baseline on the low-frequency side of the reflectivity band and should be considered in the fitting model of quasinormal reflectivity. Using REFFIT software [31], we attempted to simulate the effect of the interface with the diamond but found only a negligible effect of the diamond interface with respect to interferences and diffraction

effects dominating at low frequencies. We thus have fitted the reflectivity data at each pressure of the low-energy modes. The results for the mode frequencies are presented in Fig. 5 for modes (3)–(5). All the fit parameters are reported in the Appendix. As mentioned before, modes (3) and (5) follow the same hardening behavior when pressure is increased, while mode (4) undergoes instead a very pronounced softening of ~ 14 cm^{-1} between 1 and 10 GPa. Above 10 GPa, the evolution of the pressure dependence changes, and the frequency slowly increases with pressure. Note that there is no clear discontinuity marking the pressure-induced structural transition, which has, however, been confirmed to occur at low temperature by neutron diffraction, as well as the presence of magnetic order [37].

IV. DISCUSSION

We have shown that at ambient pressure, due to the magnetoelastic effect at the Néel temperature, phonon modes (3)–(6) (reported in Table I) clearly exhibit a deviation from the conventional anharmonic behavior, like in other magnetoelastic materials [38,39]. These modes imply strong displacements of the Fe1 and Fe2 atoms, and of the oxygens (O1, O2, and O3) mediating the superexchange paths. For modes (3), (5), and (6), the abnormal softening stops at 160 K, whereas mode (4) continues to soften until the lowest measured temperature. Besides, when the pressure is further increased in the magnetically ordered phase, one observes the expected hardening of all modes, except mode (4), which softens.

In order to understand the distinctive feature of this mode and its relevance to the structural and magnetic properties, we calculated the dynamical changes, induced by each mode, in the bond superexchange paths forming the pentagonal lattice. As reported in Fig. 6, within the pentagonal lattice,
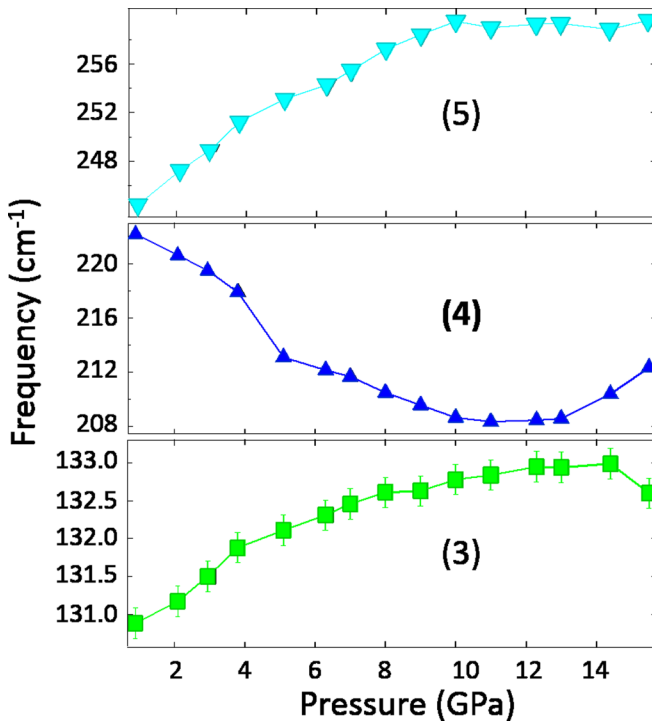

FIG. 5. Pressure dependence of frequencies of modes (3)–(5) obtained from Drude-Lorentz fits of 40-K measurements. The error bars have been estimated using the reproducibility of the fit with different numbers of oscillators. For modes (4) and (5), the errors bars are smaller than the symbols.
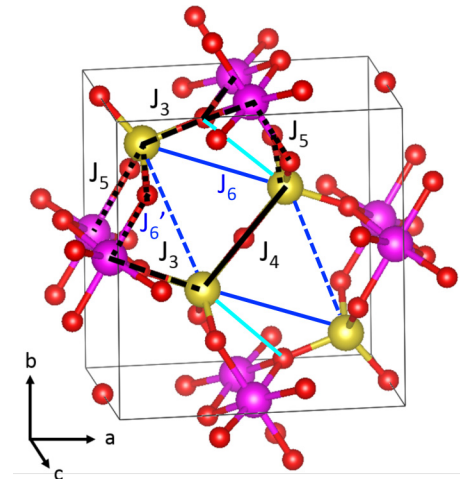
FIG. 6. Perspective view of a pentagonal slab of $Bi_2Fe_4O_9$. The Fe1 atoms (in yellow) and Fe2 atoms (in pink) magnetically interact by the superexchange interactions J_3 (long-dashed black lines), J_4 (solid black lines), and J_5 (short-dashed black lines). The second-neighbor interactions between Fe1 atoms, J_6 and J_6', are shown in dark blue, as well as the potential Fe1-O3 new atomic bond at high pressure in turquoise. For the sake of clarity the Bi atoms are absent from the drawing.

the iron atoms magnetically interact via three competing antiferromagnetic superexchange integrals, J_3, J_4, and J_5, corresponding to the exchange paths Fe1-O3-Fe2, Fe1-O1-Fe1, and Fe1-O2-Fe2, respectively. Note that two additional rather weak superexchange interactions, J_1 and J_2, are at play between the Fe2 atoms along the c axis. According to the Goodenough-Kanamori-Anderson rule [40,41], the antiferromagnetic superexchange interaction between two transition metals is the strongest when the angle is $180°$, and it weakens as the angle decreases. Moreover, the strength of the interaction increases when the bond length distance between the magnetic atom and the oxygen decreases. At equilibrium, the values of the superexchange interactions have been determined recently from inelastic neutron measurements [42]: $J_1 = 3.7$, $J_2 = 1.3$, $J_3 = 6.3$, $J_4 = 24$, and $J_5 = 2.9$ meV. The dominating antiferromagnetic interaction is J_4 as its exchange path angle is exactly $180°$ at ambient conditions.

The LDCs give us the maximal atomic displacements for each phonon mode in the low-pressure *Pbam* phase. We used these results to calculate the variation induced by each oscillation mode in the superexchange paths associated with J_3, J_4, and J_5 (angle and bond length distances) and in the Fe1-O3-Fe1 paths possibly enabling the second-neighbor interactions J_6 and J_6' between the tetrahedral irons (see Fig. 6). The changes in the superexchange angle $\Delta\alpha$ and the bond length variations Δd are given for each mode in Tables II and III. The corresponding oscillations may induce a splitting of the otherwise equivalent angle and distances of the equilibrium structure. All modes thus produce a desymmetrization of the Fe1-O1-Fe1 J_4 exchange path and two inequivalent exchange paths for J_5. For J_3, only modes (2)–(4) and (6) lead to a path splitting. The distance and angle changes associated with mode (1) are small as expected since it reflects mainly the bismuth motion. All the other modes significantly modify some of the angles and distances involved in the exchange paths of J_3, J_4, and J_5. The most important change is the systematic reduction of the Fe1-O1-Fe1 angle entering the J_4 interaction. One major crystallographic change induced by pressure is actually the kinking of the straight Fe1-O1-Fe1 angle between the FeO$_4$ tetrahedra, which is incidentally expected to weaken the J_4 interaction. It is associated with the displacement of the O1 oxygen atom from its special position on an inversion center to a less-constrained position on a mirror plane [17]. In addition to the superexchange paths related to the J_3, J_4, and J_5 pentagonal interactions, the second-neighbor Fe1-O3 distance (turquoise lines in Fig. 6) is also altered by the different phonon motions as can be seen in Table III. A sufficient reduction of this bond length is expected to enable a new superexchange interaction J_6 through the second-neighbor path Fe1-O3-Fe1.

Let us now consider the distinctive character of mode (4). It involves both iron sites Fe1 and Fe2 and all oxygen atoms involved in the pentagonal exchange paths (Table I), and it displays the minimum change of the Fe1-O1-Fe1 $180°$ angle, hence suggesting a minimum reduction of the dominant J_4 interaction (Table II). Remarkably, mode (4) is also the one involving the strongest simultaneous reduction of both Fe1-Fe1 and Fe1-O3 bond lengths and increase in the Fe1-O3-Fe1 $119°$ angle involved in the J_6 exchange path, therefore strengthening it (Table III). In particular, the second-

TABLE II. Comparison between the superexchange paths in the pentagonal lattice (Fe1-O-Fe2 for the J_3 and J_5 interactions and Fe1-O-Fe1 for the J_4 one) at equilibrium and ambient conditions and altered by the atomic vibration associated with the B_{2u} modes. The degeneracy of each motion in terms of angle and Fe-O distance is given in parentheses. The larger calculated changes are highlighted in bold.

	J_3	J_4	J_5
Equilibrium			
α (deg)	129.7 (×4)	180	119.6 (×4)
d_{Fe1-O} (Å)	1.847 (×2)	1.811 (×2)	1.901 (×4)
d_{Fe2-O} (Å)	1.972 (×4)		2.029 (×4)
Mode (1)			
$\Delta\alpha$ (deg)	−0.9 (×4)	−1.4	−0.1 (×2)
Δd_{Fe1-O} (Å)	−0.04 (×2)	±0.001	−0.003 (×2)
Δd_{Fe2-O} (Å)	−0.038 (×4)		−0.134 (×2)
$\Delta\alpha$ (deg)			+ 0.86 (×2)
Δd_{Fe1-O} (Å)			−0.018 (×2)
Δd_{Fe2-O} (Å)			+0.138 (×2)
Mode (2)			
$\Delta\alpha$ (deg)	+1.5 (×2)	**−11.7**	**+7.93** (×2)
Δd_{Fe1-O} (Å)	+0.117	+0.014/+0.006	+0.008 (×2)
Δd_{Fe2-O} (Å)	+0.081 (×2)		+0.011 (×2)
$\Delta\alpha$ (deg)	−1.5 (×2)		+0.42 (×2)
Δd_{Fe1-O} (Å)	−0.114		+0.141 (×2)
Δd_{Fe2-O} (Å)	−0.072 (×2)		+0.018 (×2)
Mode (3)			
$\Delta\alpha$ (deg)	+ 0.5 (×2)	**−10.7**	−0.32 (×2)
Δd_{Fe1-O} (Å)	+0.18	+0.014/+0.002	+0.03 (×2)
Δd_{Fe2-O} (Å)	−0.034 (×2)		−0.136 (×2)
$\Delta\alpha$ (deg)	−1.9 (×2)		**+2.86** (×2)
Δd_{Fe1-O} (Å)	−0.068		−0.027 (×2)
Δd_{Fe2-O} (Å)	+0.044 (×2)		−0.139 (×2)
Mode (4)			
$\Delta\alpha$ (deg)	**−3.8** (×2)	**−7.5**	**−3** (×2)
Δd_{Fe1-O} (Å)	+0.179	0/+0.009	−0.019 (×2)
Δd_{Fe2-O} (Å)	−0.147 (×2)		**−0.485** (×2)
$\Delta\alpha$ (deg)	**+2.4** (×2)		−0.3 (×2)
Δd_{Fe1-O} (Å)	−0.172		−0.021 (×2)
Δd_{Fe2-O} (Å)	+0.162 (×2)		**−0.488** (×2)
Mode (5)			
$\Delta\alpha$ (deg)	**−5.2** (×4)	**−28.3**	**−6.1** (×2)
Δd_{Fe1-O} (Å)	**−0.415** (×2)	+0.025/+0.089	+0.128 (×2)
Δd_{Fe2-O} (Å)	+0.062 (×4)		−0.129 (×2)
$\Delta\alpha$ (deg)			+0.74 (×2)
Δd_{Fe1-O} (Å)			−0.048 (×2)
Δd_{Fe2-O} (Å)			−0.138 (×2)
Mode (6)			
$\Delta\alpha$ (deg)	**−20.4** (×2)	**−52.8**	**−10.4** (×2)
Δd_{Fe1-O} (Å)	+0.798	0.27/+0.152	+0.136 (×2)
Δd_{Fe2-O} (Å)	−0.093 (×2)		−0.153 (×2)
$\Delta\alpha$ (deg)	**+6.44** (×2)		**−2.23** (×2)
Δd_{Fe1-O} (Å)	**−0.707**		**0.247** (×2)
Δd_{Fe2-O} (Å)	**+0.322** (×2)		−0.145 (×2)

neighbor Fe1-O3 bond length decreases from the equilibrium value of 3.02 to 2.69 Å, which may allow this O3 to enter in the coordination sphere of the Fe1 atom. Concerning the J_6' interaction, the second-neighbor Fe1-O3 bond length also

TABLE III. Comparison between the superexchange paths Fe1-O3-Fe1 involved in J_6 and J'_6 interactions at equilibrium and ambient conditions and altered by the atomic vibration associated with the B_{2u} modes. The simultaneous decrease in the Fe1-Fe1 and Fe1-O3 bond length and increase in Fe1-O3-Fe1 angle of interaction J_6 are highlighted in bold.

	J_6	J'_6
Equilibrium		
$d_{\text{Fe1-Fe1}}$ (Å)	4.241	4.531
$d_{\text{Fe1-O3}}$ (Å)	3.021	3.641
$d_{\text{O3-Fe1}}$ (Å)	1.847	1.847
α (deg)	119.2	106.7
Mode (1)		
$\Delta d_{\text{Fe1-Fe1}}$ (Å)	+0.004/−0.005	+0.012/−0.012
$\Delta d_{\text{Fe1-O3}}$ (Å)	−0.03/+0.027	−0.06/+0.059
$\Delta d_{\text{O3-Fe1}}$ (Å)	−0.04/+0.042	+0.042/−0.04
$\Delta \alpha$ (deg)	+3.1/−3	+1.6/−1.7
Mode (2)		
$\Delta d_{\text{Fe1-Fe1}}$ (Å)	−0.12/+0.146	−0.36/+0.361
$\Delta d_{\text{Fe1-O3}}$ (Å)	−0.25/+0.259	−0.05/+0.286
$\Delta d_{\text{O3-Fe1}}$ (Å)	+0.107/−0.11	−0.08/+0.117
$\Delta \alpha$ (deg)	+1.1/−0.3	−0.9/+0.9
Mode (3)		
$\Delta d_{\text{Fe1-Fe1}}$ (Å)	−0.14/+0.194	−0.46/+0.465
$\Delta d_{\text{Fe1-O3}}$ (Å)	0.0/−0.002	−0.023/+0.022
$\Delta d_{\text{O3-Fe1}}$ (Å)	+0.18/−0.07	−0.07/+0.18
$\Delta \alpha$ (deg)	−12.4/+0.9	−15.2/+13.4
Mode (4)		
$\Delta d_{\text{Fe1-Fe1}}$ (Å)	**−0.16**/+0.231	−0.53/+0.544
$\Delta d_{\text{Fe1-O3}}$ (Å)	**−0.33**/+0.459	−0.73/+0.738
$\Delta d_{\text{O3-Fe1}}$ (Å)	**−0.17**/+0.179	+0.179/−0.17
$\Delta \alpha$ (deg)	**+17.4**/−13.6	+0.1/−1.8
Mode (5)		
$\Delta d_{\text{Fe1-Fe1}}$ (Å)	−0.021/+0.021	−0.056/+0.057
$\Delta d_{\text{Fe1-O3}}$ (Å)	+0.093/−0.02	−0.36/+0.315
$\Delta d_{\text{O3-Fe1}}$ (Å)	−0.42/+0.424	+0.456/−0.42
$\Delta \alpha$ (deg)	+13.6/−12.1	−1.5/+0.5
Mode (6)		
$\Delta d_{\text{Fe1-Fe1}}$ (Å)	−0.1/+0.111	−0.3/+0.279
$\Delta d_{\text{Fe1-O3}}$ (Å)	−0.88/+0.905	−0.32/+0.488
$\Delta d_{\text{O3-Fe1}}$ (Å)	+0.798/−0.71	−0.72/+0.798
$\Delta \alpha$ (deg)	+0.2/−14.8	+32.8/−19.1

decreases significantly but only to reach $\approx$2.9 Å, which remains out of the coordination sphere of the Fe1. Note that mode (4) softening under pressure is as large as 7%, while its softening below T_N is only 0.5%. These softenings imply that the atomic motions of mode (4) are energetically favored by the application of pressure as well as by the magnetic ordering. Actually, according to Friedrich *et al.* [17], the driving force of the structural transition, also observed in $Bi_2Ga_4O_9$ at higher pressure, is the tendency of Fe^{3+} and Ga^{3+} in tetrahedral coordination towards a higher coordination than 4 on pressure increase. For mode (6), the second-neighbor Fe1-O3 bond length also decreases, but this is concomitant with an increase of the first-neighbor Fe1-O3 bond length entering the J_6 interaction. Thus the dynamical increase in

oxygen coordination is clearly a specificity of mode (4). On the magnetic side, it means that another exchange path (J_6) could be enabled between second Fe1 neighbors, which is expected to modify the magnetic order in the high-pressure phase. Friedrich *et al.* have also pointed out the flexibility of the J_4 interactions under pressure, which is confirmed by the strong decrease in the Fe1-O1-Fe1 angle in all modes. However, this change is minimal for mode (4), which might indicate that in the magnetically ordered phase, the bending of the J_4 angle is opposed by magnetostrictive effects.

Globally, these results highlight the interplay between magnetism and atomic motions. As a consequence, the magnetic structure stabilized at ambient pressure below T_N could be strongly modified in the pressure-induced phase. Indeed, the change in the J_4 interaction as well as the possibility of new exchange paths can release the frustration at the origin of the peculiar 90° magnetic structure. Modifications in the magnetic structure under pressure have actually been observed in related compounds of the RMn_2O_5 family with R being a rare-earth atom [43,44]. They crystallize in the same space group, forming pentagons of Mn^{3+} and Mn^{4+}, where the Mn tetrahedra are connected by two oxygens instead of one as in $Bi_2Fe_4O_9$. No pressure-induced structural transition has been reported yet for most members of the family, but they present magnetically induced ferroelectricity which is also modified under pressure. Associated with the expected change in the magnetic structure, one may thus wonder about the possibility of magnetically induced ferroelectricity under pressure in $Bi_2Fe_4O_9$ as well.

V. CONCLUSION

In summary, we have reported the infrared spectrum of the pentagonal antiferromagnet $Bi_2Fe_4O_9$ as a function of temperature and pressure and identified strong signatures of magnetoelastic effects. One peculiar phonon around 225 cm^{-1} presents an abnormal softening both in temperature and pressure. This mode involves atomic displacements of all Fe and O in each pentagonal plane; it also dynamically favors an increase in coordination of the tetrahedral irons, which is expected to be the driving mechanism responsible for the pressure-induced structural transition earlier reported. This is expected to modify significantly the respective strength of the competing magnetic interactions in $Bi_2Fe_4O_9$, and we therefore anticipate important modifications of the magnetic structure at high pressure in this remarkable material.

TABLE IV. Ambient pressure DL phonon parameters for modes (1)–(6) obtained from the fits of the reflectivity measured at selected temperatures.

	Mode (1)			Mode (2)			Mode (3)			Mode (4)			Mode (5)			Mode (6)		
T (K)	Ω (cm^{-1})	γ (cm^{-1})	$\Delta\epsilon$	Ω (cm^{-1})	γ (cm^{-1})	$\Delta\epsilon$	Ω (cm^{-1})	γ (cm^{-1})	$\Delta\epsilon$	Ω (cm^{-1})	γ (cm^{-1})	$\Delta\epsilon$	Ω (cm^{-1})	γ (cm^{-1})	$\Delta\epsilon$	Ω (cm^{-1})	γ (cm^{-1})	$\Delta\epsilon$
20	69.6	2.1	2.08	111.3	3.8	0.55	131.7	4.2	2.00	224.6	4.1	0.89	242.1	6.0	0.79	311.3	5.3	0.35
50	69.7	2.0	2.01	111.4	3.7	0.55	131.6	4.2	2.07	224.6	4.3	0.95	241.8	6.1	0.82	311.1	5.8	0.39
100	69.7	2.1	2.43	111.3	3.9	0.70	130.8	3.9	2.61	224.3	4.5	1.37	240.5	6.2	1.09	309.9	8.9	0.83
150	69.5	2.1	2.74	111.0	4.9	0.95	129.7	4.1	2.91	224.7	5.2	1.41	239.9	6.8	1.20	309.3	12.6	1.18
200	69.2	2.2	2.93	110.6	8.3	1.37	128.9	4.5	2.87	225.4	6.1	1.13	239.9	7.7	1.14	310.1	9.7	0.88
220	69.2	2.7	2.39	110.5	9.8	1.06	129.2	5.2	2.29	226.0	6.9	0.73	240.7	8.3	0.82	310.8	9.5	0.36
230	69.1	2.7	2.67	110.6	7.2	0.85	129.3	4.9	2.60	225.6	7.4	0.98	240.1	8.5	0.95	310.8	9.2	0.42
240	69.0	2.8	2.88	110.6	6.9	0.82	129.2	4.8	2.71	225.6	7.4	1.00	240.0	8.2	0.98	310.8	8.2	0.37
250	69.0	2.6	2.81	110.6	6.7	0.82	129.0	4.7	2.77	225.3	7.9	1.13	239.6	8.6	0.98	310.6	9.5	0.44
300	68.9	2.8	2.98	110.5	6.9	0.90	128.3	4.8	3.08	224.9	8.6	1.33	238.5	9.3	1.06	310.1	10.4	0.44

APPENDIX

Bi$_2$Fe$_4$O$_9$ reflectivity spectra at different temperatures and pressures have been fitted using the Drude-Lorentz model with REFFIT software [31]. More details on the fits and the associated parameters are reported in this Appendix.

The Drude-Lorentz model describes the optical response of an insulator with a set of harmonic oscillators for each phonon mode. The dielectric constant is given by

$$\epsilon(\omega) = \epsilon_\infty + \sum_k \frac{\Delta\epsilon_k \Omega_k^2}{\Omega_k^2 - \omega^2 - i\gamma_k\omega}. \tag{A1}$$

ϵ_∞ is the so-called "high-frequency dielectric constant," which represents the contribution of all oscillators at very high frequencies. The parameters Ω_k, $\Delta\epsilon_k$, and γ_k are the resonance frequency, the oscillator strength, and the linewidth, respectively, of the kth Lorentz oscillator.
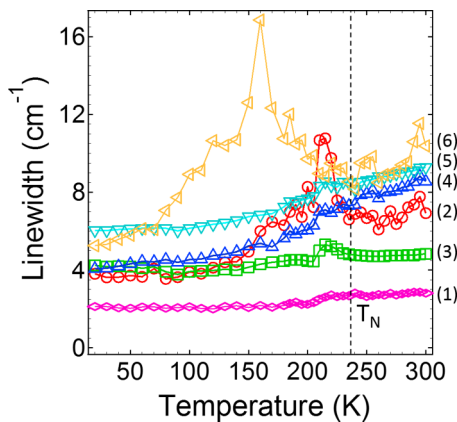
The DL fit parameters at selected temperatures and ambient pressure are given in Table IV for modes (2)–(6). In Fig. 7, their linewidths are plotted as a function of temperature. Mode (6) is anomalously large from 200 K down to 60 K. It involves Fe1 as well as O1 and O3 atomic sites. Mode (2) presents a much sharper anomaly just below T_N: This mode involves only Fe1 and O1, which corresponds to the strongest antiferromagnetic bound. Modes (1) and (3)–(5) have weaker temperature dependencies.

In Table V are reported the DL phonon parameters obtained from the reflectivity measured at 40 K and different pressures. The fits have been performed for modes (3)–(5). Their linewidths are plotted in Fig. 8 as a function of pressure up to 15.5 GPa. No clear anomaly is observed, but there is an overall tendency to an increase with increased pressure, with an upturn above 9 GPa.

FIG. 7. Linewidth γ of modes B$_{2u}$(1), B$_{2u}$(2), B$_{2u}$(3), B$_{2u}$(4), B$_{2u}$(5), and B$_{2u}$(6) as a function of temperature. The dashed line represents the Néel temperature of the sample, $T_N = 238$ K.
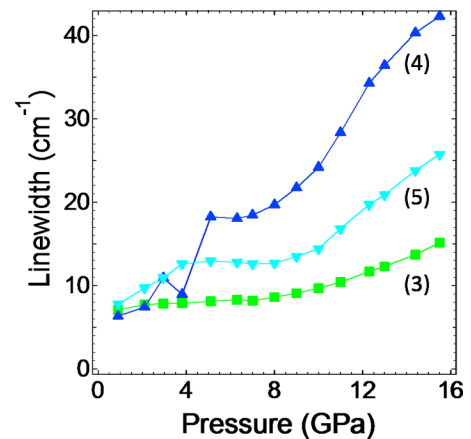
FIG. 8. Pressure dependence of linewidths (γ) of modes B$_{2u}$(3), B$_{2u}$(4) and B$_{2u}$(5) of Bi$_2$Fe$_4$O$_9$ obtained from the Drude-Lorentz fits of measurements performed at T = 40 K as a function of pressure.

TABLE V. Phonon parameters obtained from the fits of the reflectivity measured at 40 K for different values of pressure.

P (GPa)	Mode (3)			Mode (4)			Mode (5)		
	Ω (cm^{-1})	γ (cm^{-1})	$\Delta\epsilon$	Ω (cm^{-1})	γ (cm^{-1})	$\Delta\epsilon$	Ω (cm^{-1})	γ (cm^{-1})	$\Delta\epsilon$
0.9	130.9	7.1	0.42	222.2	6.3	0.22	244.4	7.8	0.19
2.1	131.2	7.7	0.44	220.6	7.4	0.23	247.2	9.7	0.18
3.0	131.5	7.8	0.48	219.5	10.9	0.26	248.9	10.9	0.20
3.8	131.9	7.9	0.49	217.9	8.9	0.28	251.2	12.6	0.22
5.1	132.1	8.1	0.50	213.1	18.2	0.42	253.1	12.9	0.24
6.3	132.3	8.3	0.52	212.1	18.0	0.42	254.3	12.8	0.25
7	132.5	8.2	0.53	211.7	18.4	0.44	255.5	12.6	0.25
8	132.6	8.6	0.55	210.5	19.7	0.47	257.3	12.7	0.27
9	132.6	9.1	0.55	209.6	21.7	0.49	258.5	13.5	0.28
10	132.8	9.7	0.56	208.6	24.2	0.51	259.6	14.4	0.29
11	132.8	10.4	0.56	208.3	28.3	0.54	259.0	16.8	0.29
12.3	133.0	11.7	0.57	208.4	34.3	0.62	259.3	19.7	0.29
13	132.9	12.3	0.58	208.6	36.4	0.65	259.4	20.9	0.28
14.4	133.0	13.7	0.60	210.4	40.3	0.69	258.9	23.8	0.28
15.5	132.6	15.1	0.65	212.3	42.3	0.66	259.6	25.7	0.26

[1] J. S. Gardner, S. R. Dunsiger, B. D. Gaulin, M. J. P. Gingras, J. E. Greedan, R. F. Kiefl, M. D. Lumsden, W. A. MacFarlane, N. P. Raju, J. E. Sonier, I. Swainson, and Z. Tun, Phys. Rev. Lett. **82**, 1012 (1999).

[2] S. T. Bramwell, Science **294**, 1495 (2001).

[3] G. R. Blake, L. C. Chapon, P. G. Radaelli, S. Park, N. Hur, S.-W. Cheong, and J. Rodriguez-Carvajal, Phys. Rev. B **71**, 214402 (2005).

[4] L. C. Chapon, G. R. Blake, M. J. Gutmann, S. Park, N. Hur, P. G. Radaelli, and S.-W. Cheong, Phys. Rev. Lett. **93**, 177402 (2004).

[5] T. Kimura, T. Goto, H. Shintani, K. Ishizaka, T. Arima, and Y. Tokura, Nature (London) **426**, 55 (2003).

[6] T. Lottermother, T. Lonkai, U. Amann, D. Hohlwein, J. Ihringer, and M. Fiebig, Nature (London) **430**, 541 (2004).

[7] M. Mostovoy, Phys. Rev. Lett. **96**, 067601 (2006).

[8] K. Wang, J.-M. Liu, and Z. Ren, Adv. Phys. **58**, 321 (2009).

[9] I. A. Sergienko and E. Dagotto, Phys. Rev. B **73**, 094434 (2006).

[10] I. A. Sergienko, C. Sen, and E. Dagotto, Phys. Rev. Lett. **97**, 227204 (2006).

[11] D. Khomskii, Physics **2**, 20 (2009).

[12] E. Ressouche, V. Simonet, B. Canals, M. Gospodinov, and V. Skumryev, Phys. Rev. Lett. **103**, 267204 (2009).

[13] I. Rousochatzakis, A. M. Lauchli, and R. Moessner, Phys. Rev. B **85**, 104415 (2012).

[14] K. S. Raman, R. Moessner, and S. L. Sondhi, Phys. Rev. B **72**, 064413 (2005).

[15] A. K. Singh, S. D. Kaushik, B. Kumar, P. K. Mishra, A. Venimadhav, V. Siruguri, and S. Patnaik, Appl. Phys. Lett. **92**, 132910 (2008).

[16] Z. M. Tian, S. L. Yuan, X. L. Wang, X. F. Zheng, S. Y. Yin, C. H. Wang, and L. Liu, J. Appl. Phys. (Melville, NY) **106**, 103912 (2009).

[17] A. Friedrich, J. Biehler, W. Morgenroth, L. Wiehl, B. Winkler, M. Hanfland, M. Tolkiehn, M. Burianek, and M. Mühlberg, J. Phys.: Condens. Matter **24**, 145401 (2012).

[18] A. Voute, M. Deutsch, A. Kalinko, F. Alabarse, J.-B. Brubach, F. Capitani, M. Chapuis, V. Ta Phuoc, R. Sopracase, and P. Roy, Vib. Spectrosc. **86**, 17 (2016).

[19] D. J. Lockwood and M. G. Cottam, J. Appl. Phys. (Melville, NY) **64**, 5876 (1988).

[20] A. B. Kuz'menko, D. van der Marel, P. J. M. van Bentum, E. A. Tishchenko, C. Presura, and A. A. Bush, Phys. Rev. B **63**, 094303 (2001).

[21] R. Schleck, R. L. Moreira, H. Sakata, and R. P. S. M. Lobo, Phys. Rev. B **82**, 144309 (2010).

[22] R. Schleck, Y. Nahas, R. P. S. M. Lobo, J. Varignon, M. B. Lepetit, C. S. Nelson, and R. L. Moreira, Phys. Rev. B **82**, 054412 (2010).

[23] R. P. S. M. Lobo, R. L. Moreira, D. Lebeugle, and D. Colson, Phys. Rev. B **76**, 172105 (2007).

[24] M. N. Iliev, A. P. Litvinchuk, V. G. Hadjiev, M. M. Gospodinov, V. Skumryev, and E. Ressouche, Phys. Rev. B **81**, 024302 (2010).

[25] C. C. Homes, M. Reedyk, D. A. Cradles, and T. Timusk, Appl. Opt. **32**, 2976 (1993).

[26] J. D. Gale, J. Chem. Soc., Faraday Trans. **93**, 629 (1997).

[27] V. N. Popov, J. Phys.: Condens. Matter **7**, 1625 (1995).

[28] A. P. litvinchuk, M. N. Iliev, V. N. Popov, and M. M. Gospodinov, J. Phys.: Condens. Matter **16**, 809 (2004).

[29] M. N. Iliev, M. V. Abrashev, A. P. Litvinchuk, V. G. Hadjiev, H. Guo, and A. Gupta, Phys. Rev. B **75**, 104118 (2007).

[30] A. P. Litvinchuk, J. Magn. Magn. Mater. **321**, 2373 (2009).

[31] A. B. Kuzmenko, Rev. Sci. Intrum. **76**, 083108 (2005).

[32] D. Voll, A. Beran, and H. Schneider, Phys. Chem. Miner. **33**, 623 (2006).

[33] T. Debnath, C. Rüscher, P. Fielitz, S. Ohmann, and G. Borchardt, J. Solid State Chem. **183**, 2582 (2010).

[34] N. Shamir, E. Gurewitz, and H. Shaked, Acta Crystallogr., Sect. A: Cryst. Phys., Diffr., Theor. Gen. Crystallogr. **34**, 662 (1978).

[35] M. Balkanski, R. F. Wallis, and E. Haro, Phys. Rev. B **28**, 1928 (1983).

[36] B. Langerome, M. Verseils, F. Capitani, J.-B. Brubach, E. Amzallag, E. Calandrini, J. Creuze, and P. Roy, J. Phys. Chem. C **123**, 15724 (2019).

[37] K. Beauvois (private communication).

[38] J. Cao, L. I. Vergara, J. L. Musfeldt, A. P. Litvinchuk, Y. J. Wang, S. Park, and S.-W. Cheong, Phys. Rev. B **78**, 064307 (2008).

[39] J. Cao, L. I. Vergara, J. L. Musfeldt, A. P. Litvinchuk, Y. J. Wang, S. Park, and S.-W. Cheong, Phys. Rev. Lett. **100**, 177205 (2008).

[40] J. B. Goodenough, Phys. Rev. **100**, 564 (1955).

[41] P. W. Anderson, Phys. Rev. **79**, 350 (1950).

[42] K. Beauvois, V. Simonet, S. Petit, J. Robert, F. Bourdarot, M. Gospodinov, A. A. Mukhin, R. Ballou, V. Skumryev, and E. Ressouche, Phys. Rev. Lett. **124**, 127202 (2020).

[43] M. Deutsch, W. Peng, P. Foury-Leylekian, V. Baledent, S. Chattopadhyay, M. T. Fernandez-Diaz, T. C. Hansen, A. Forget, D. Colson, M. Greenblatt, M.-B. Lepetit, S. Petit, and I. Mirebeau, Phys. Rev. B **98**, 024408 (2018).

[44] W. Peng, V. Baledent, C. V. Colin, T. C. Hansen, M. Greenblatt, and P. Foury-Leylekian, Phys. Rev. B **99**, 245109 (2019).